Catalytic screening of phosphate-based Pt catalysts: Understanding the influence of the support

S. Navarro-Jaén, M.A. Centeno, F. Romero-Sarria, O. H. Laguna, J. A. Odriozola

Departamento de Química Inorgánica e Instituto de Ciencia de Materiales de Sevilla, Centro mixto Universidad de Sevilla-CSIC, Av. Américo Vespucio 49, 41092 Seville, Spain

1.   Introduction

The water gas shift reaction (WGS, $CO + H_2O \leftrightarrow CO_2 + H_2$) is a well-known reaction implied, among others, in the hydrogen clean-up process for its subsequent use as feed for polymer electrolyte membrane fuel cells (PEMFCs) [1-5]. The advantages concerning the use of supported noble metals catalysts have motivated a deep study of these materials over the years, regarding both the employed metal phase and the support [4, 6-8]. A general conclusion derived from the numerous studies accomplished is the synergy existing between the active phase and the support [9-12]. The latter is involved in the activation of the water molecule, generally recognized as the rate-limiting step of the WGS reaction [13-15]. Both reducible and non-reducible oxide-type supports have been extensively studied for the WGS reaction [3, 7, 16-19]. Among them, CeO_2 has been proposed as an interesting candidate since it greatly enhances the water activation rate through the influence of its electronic properties (the redox pair Ce^{3+}/Ce^{4+}), directly related with the presence of oxygen vacancies in the solid. Consequently, CeO_2 has been used both alone or as promoter of Al_2O_3 supported Pt catalysts [12, 14]. González-Castaño et al. [10] improved the formulation of the CeO_2/Al_2O_3 (CeAl) support by adding Zr and Fe dopants, which provoke a modification on the redox properties of the support and facilitates the water activation step. Additionally, the combination of Zr and Fe demonstrated to inhibit the carbon deposits formation on the catalyst surface.

Afterwards, García-Moncada et al. [13, 20] introduced the use of a physical mixture of protonic conductors to a typical Pt/CeAl catalyst, generated by aliovalent doping of transition or rare earth metal oxides, which improves the WGS catalytic performance through a proton conduction mechanism, promoting the water dissociation step. Considering the aforementioned results, we evaluated the use of $CePO_4$ as supports for Pt catalysts, considering the presence of cerium in its structure and its previous use as protonic conductor in fuel cells [21]. A wide range of phosphate-type systems have been used for fuel cell applications, where the proton transport is generally described on the basis of two mechanisms: the "Grotthus mechanism", which implies protons hopping and the "diffusion mechanism", which establishes the water molecule as proton vehicle [22, 23]. Thus, phosphate-systems transport properties observed on these membranes were successfully adapted to WGS catalytic systems through the use of $CePO_4$. The main potential of this type of materials lies in the possibility of tuning their chemical and structural properties and consequently, their textural and surface properties. In this sense, the texture of the support, especially its porosity, influences both their adsorption and ion-exchange abilities [24-26], whereas the selection of the metal cation and the inorganic anion becomes crucial for the effective control of the surface acid-base properties [27]. Due to these exceptional tunable properties [21], an extrapolation of these results can be applied to another phosphate-type systems.

In this work, a series of phosphate-type materials containing different cations (Ce, Ca and Ti) have been synthesized and evaluated as supports of 2 wt. % Pt catalysts. The water availability in the supports and their structure are correlated with the WGS catalytic performance.

2.   Materials and methods

2.1.   Supports and catalysts synthesis

A series of phosphate-type supports containing different cations (Ce, Ca and Ti) were prepared by a hydrothermal method, with nominal molar ratios Ce/P 1:1, Ca/P 1.67:1 and Ti/P 1:1. The obtained solids were labelled as CeP, CaP and TiP respectively.

The synthesis of CeP and CaP were carried out by a hydrothermal method previously described [21, 28]. 50 ml of aqueous solutions of phosphoric acid 85% (Panreac) 0.6 M and cerium (III) nitrate (Fluka) 0.6 M (CeP) or calcium nitrate tetrahydrate (VWR) 1 M (CaP) were mixed in a flask and stirred at 40 °C. Then, 50 ml of an aqueous solution of sodium citrate dihydrate (Sigma) 0.019 M (CeP) or 0.017 M (CaP) was added and the pH was adjusted to 10 by means of the addition of ammonia 30%. The resultant solution was maintained at 40 °C for 8 hours under stirring and finally transferred to a Teflon-lined autoclave, in which the mixture was aged at 100 °C for 8 hours. The material was finally filtered, washed with distilled water and dried overnight at 100 °C. The solid CeP was divided in two fractions and calcined at 400 and 600 °C, denominated CeP400 and CeP600, whereas the solid CaP was calcined at 350 °C.

The synthesis of TiP was carried out by means of an adapted hydrothermal method [29]. 50 ml of a phosphoric acid 85% (Panreac) aqueous solution 0.7 M were mixed with $6 \cdot 10^{-4}$ moles of P123 (BASF) and maintained under stirring until complete dissolution of the surfactant. 0.04 moles of $C_{12}H_{29}O_4Ti$ (Aldrich) were then added and the resultant solution was stirred for 2 hours. The mixture was sealed in a Teflon-lined autoclave and aged at 80 °C for 24 h. The obtained product was filtered, washed with water, dried overnight at 60 °C and finally calcined to 600 °C.

The Pt catalysts with a nominal metal content of 2 wt.% were prepared by the wet impregnation method. For this purpose, an aqueous solution of $Pt(NH_3)_4(OH)_2$ 0.053 M was prepared, and the corresponding amount of support was added. The mixture was

maintained under stirring for 24 hours and dried at 60 °C. Finally, the obtained catalysts were calcined at 350 °C for 2 hours.

2.2.   Supports and catalysts characterization

Powder X-ray diffraction patterns were collected on a Panalytical X'PERT PRO diffractometer using CuKα radiation (40 mA, 45 kV). The sample patterns were recorded in the 10-90 °2θ range with 0.05° step size and 300 s of step time.

Chemical composition of the prepared samples was analyzed by Inductively Coupled Plasma Atomic Emission Spectrometry (ICP-AES) on a Horiba Jobin Yvon spectrometer, after HF acid digestion of the samples.

Textural properties of the solids were evaluated by N_2 adsorption-desorption experiments at liquid nitrogen temperature in a Micromeritics TriStar II 3020 apparatus. Prior to the experiment, samples were degassed at 250 °C for 2 hours under vacuum.

Transmission electron microscopy (TEM) micrographs of the catalysts were obtained in a PHILIPS CM-200 transmission electron microscope, equipped with microanalysis (EDS) with a minimum step size of 15 nm and 2.8 Å of maximum resolution between two points.

Adsorption of water on the prepared supports was followed by in situ diffuse reflectance infrared spectroscopy (DRIFTS) in a high-temperature reaction chamber attached on a Praying Mantis (Harrick) DRIFTS optical system with ZnSe windows. Spectra were collected by a Thermo Nicolet iS50 FT-IR spectrometer equipped with a liquid-nitrogen cooled MCT detector, at a resolution of 4 cm^{-1} and an average of 64 scans. The outlet gas composition was analyzed in an on-line connected FEIFFER mass spectrometer Vacuum Prisma Plus controlled by the Quadera® software. For every experiment, 40 mg of the solids were finely ground and loaded in the catalytic cell. The samples were first activated at the calcination temperature under a 10% H_2/Ar flow for 1 hour and submitted

to a 10% H_2O/Ar feed-stream (50 ml·min^{-1}) using a KNAUER Smartline 1050 HPLC pump and a series of AALBORG mass-flow controllers. The experiments were performed in the range of temperature between 150 and 350 °C. All the pipelines of the system were heated at 100 °C to avoid water condensation during the analysis.

2.3. Catalytic test

WGS reaction was carried out at atmospheric pressure on a cylindrical Hastelloy reactor (i.d. 17 mm). For every reaction, 200 mg of the powder catalyst (ø = 600-800 μm) were diluted with SiC to generate a catalyst bed volume of 6 cm^3. Samples were firstly pretreated at 350 °C under a 10% H_2/N_2 flow with a total rate of 100 ml·min^{-1}. The catalysts were then submitted to 100 ml·min^{-1} of a typical WGS feed-stream (7 vol.% CO, 9 vol.% CO_2, 50 vol.% H_2, 30 vol.% H_2O and 4 vol.% N_2). Reactants and products were analyzed by gas chromatography in a VARIAN CP-4900 μGC equipped with a ®Porapak Q column, a Mole-Sieve 5A and two TCD detectors. Additionally, a direct recording of the CO_2 vol.% at the reactor outlet was followed using a VAISALA GMT220 series detector. CO conversion was calculated according to Eq. 1. For sake of comparison, low and medium temperature Cu-based commercial catalysts were also evaluated.

$$X_{CO}(\%) = \frac{F_{CO\ in} - F_{CO\ out}}{F_{CO\ in}} x100 \qquad (1)$$

Where $F_{CO\ in}$ and $F_{CO\ out}$ are the inlet and outlet volume of CO in the reactor, respectively.

3. Results and discussion

3.1. Characterization results

Table 1 summarizes the physicochemical properties of the prepared solids. Specific surface area values of the supports are in the range between 41 and 248 m^2 g^{-1}, being that of TiP significantly higher compared to the other prepared supports. Pore volume values are comprised between 0.32 and 0.62 cm^3 g^{-1}, corresponding the maximum value

to TiP. After Pt deposition and calcination, no significative changes on these values are observed, being similar to those of the supports. Regarding the cation/phosphorous (C/P) molar ratio of the supports, the values obtained are those expected from the synthesis procedure except for the solid TiP, which indicates that a loss of phosphorous has taken place in this solid.

Table 1. Physicochemical properties of the supports and catalysts.

Sample	S_{BET} ($m^2 g^{-1}$)	V_p ($cm^3 g^{-1}$)	D_p (nm)	Pt mean particle size (nm)[b]	Metal loading (wt %)	C/P ratio
CeP400[a]	65	0.32	17.2	-	-	-
CeP600[a]	41	0.35	28.2	-	-	-
CaP	69	0.39	16.8	-	-	-
TiP	248	0.62	8.5	-	-	-
Pt/CeP400[a]	71	0.32	16.6	1	1.5	1
Pt/CeP600[a]	44	0.30	23.2	1.2	1.4	1
Pt/CaP	73	0.47	19.4	0.7	1.4	1.7
Pt/TiP	246	0.58	8.2	2.6	1.6	2.2

[a] Previously reported in Ref. [21]

[b] Calculated from TEM micrographs

X-ray diffraction patterns of the prepared solids are shown in Figure 1. The support CeP400 present the diffraction lines corresponding to the rhabdophane-type phase of $CePO_4$ ($CePO_4 \cdot 0.53H_2O$), which is known to present structural channels (JCPDS-ICDD 01-075-1880), whereas the crystallographic pattern of the support CeP600 corresponds to the monazite-type phase of the $CePO_4$ (JCPDS-ICDD 01-077-0429), emerging from the dehydration of the rhabdophane-type phase and where the structural channels are missed [30-32]. Detailed descriptions of these structures have been previously reported [21]. The diffraction pattern of CaP corresponds to the hexagonal calcium hydroxyapatite structure ($P6_3/m$ space group), with formula $Ca_{10}(PO_4)_6(OH)_2$ (JCPDS-ICDD 01-074-0566). According to the literature, the hydroxyapatite framework is constituted by the assembly of calcium ions and tetrahedral phosphate groups delimiting two types of unconnected channels oriented along the c axis: one of them has a diameter of 2.5 Å and is bordered by calcium ions, and the second one possesses a diameter of

approximately 3.5 Å and is bordered not only by calcium ions but also by oxygen atoms. These channels contain the structural OH groups which balance the positive charge of the compound [33, 34]. Conversely to the previous supports, the support TiP presents a low degree of crystallinity. The amorphization degree of TiP have been previously related to the time and temperature conditions of the hydrothermal method employed during the synthesis [35, 36]. Nevertheless, it is possible to distinguish a broad diffraction line at 25.2 °2θ, related to the presence of the anatase phase of TiO_2 (JCPDS-ICDD 00-002-0387). Although the anatase-rutile transition phase takes place between 500 and 600 °C, the presence of phosphorous has demonstrated to increase the thermal stability of the anatase phase [37], which explains the presence of this phase after calcination at 600 °C. Additionally, a diffraction peak at 22.4 °2θ, corresponding to the most intense diffraction line of TiP_2O_7 (JCPDS-ICDD 00-038-1468) is observed. Thus, this solid consists in a mixture of TiP_2O_7 and TiO_2, in good agreement with the loss of phosphorous induced by the calcination treatment revealed by chemical analysis. After Pt deposition and calcination of the solids, no diffraction lines corresponding to Pt species are observed, indicating the small particle size of the metallic particles in all the samples. Nevertheless, the catalyst Pt/TiP presents an increase of the diffraction peak at 25.2 °2θ, suggesting that the segregation of anatase occurs after Pt deposition and calcination.
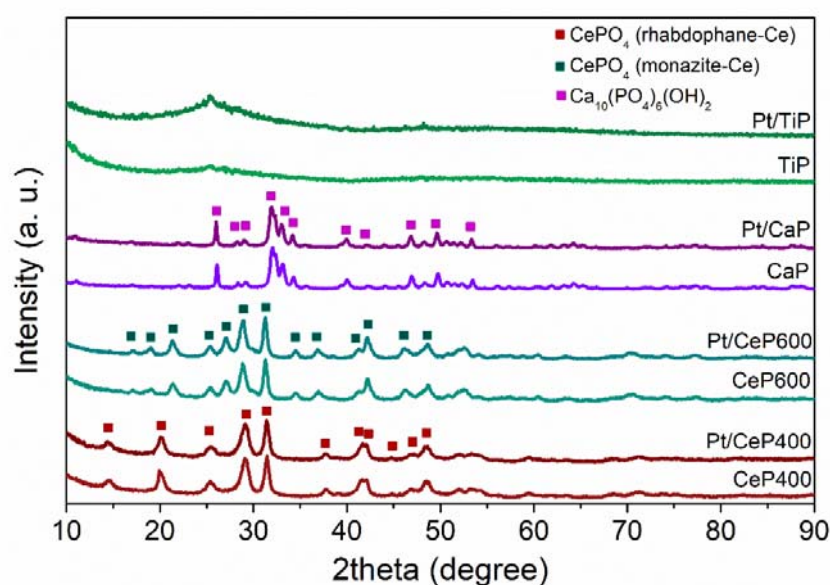
Figure 1. XRD patterns of the prepared solids.

Figure 2 presents the N_2 adsorption/desorption isotherms and the BJH pore size distribution curves of the supports after calcination. Figure 2a shows that supports containing Ce and Ca present a pronounced N_2 uptake at $p/p_0 \approx 0.8$, indicating that multilayer adsorption starts at high relative pressure in these solids. However, the adsorption isotherm of the support TiP shows a superior N_2 uptake capacity from $p/p_0 \approx$ 0.5, thus pointing out that this material exhibits a high microporosity feature. In addition, the middle section of the curve is less defined that in the other supports, which shows that formation of mono- and multilayer are overlapped. Considering the hysteresis loop, both CeP supports present a H1 hysteresis, typical of solids containing uniform channels, as in the support CeP400 or constituted by aggregates of particles, as in CeP600. The solid CaP gives rise to a H2 hysteresis, characteristic of solids containing cylindrical channels with non-uniform size and shape, being consistent with the description of the hydroxyapatite structure in which two types of structural channels have been described [34, 38]. The solid TiP presents a H3 hysteresis, typically found in non-rigid aggregates of particles and thus, not representing a reliable description of the porosity of the material [39, 40]. According to the BJH pore size distribution derived from the desorption brand of the isotherm (Fig. 2b), the mesopore volume decreases in the order: CaP > CeP400 > CeP600 > TiP, which is in agreement with the description of the supports features shown in Table 1. This reduction of the mesopore volume is accompanied by a broadening of the pore size distribution. After Pt deposition, the evolution of the adsorption isotherms and the pore size distribution follow the same trend observed for the supports.
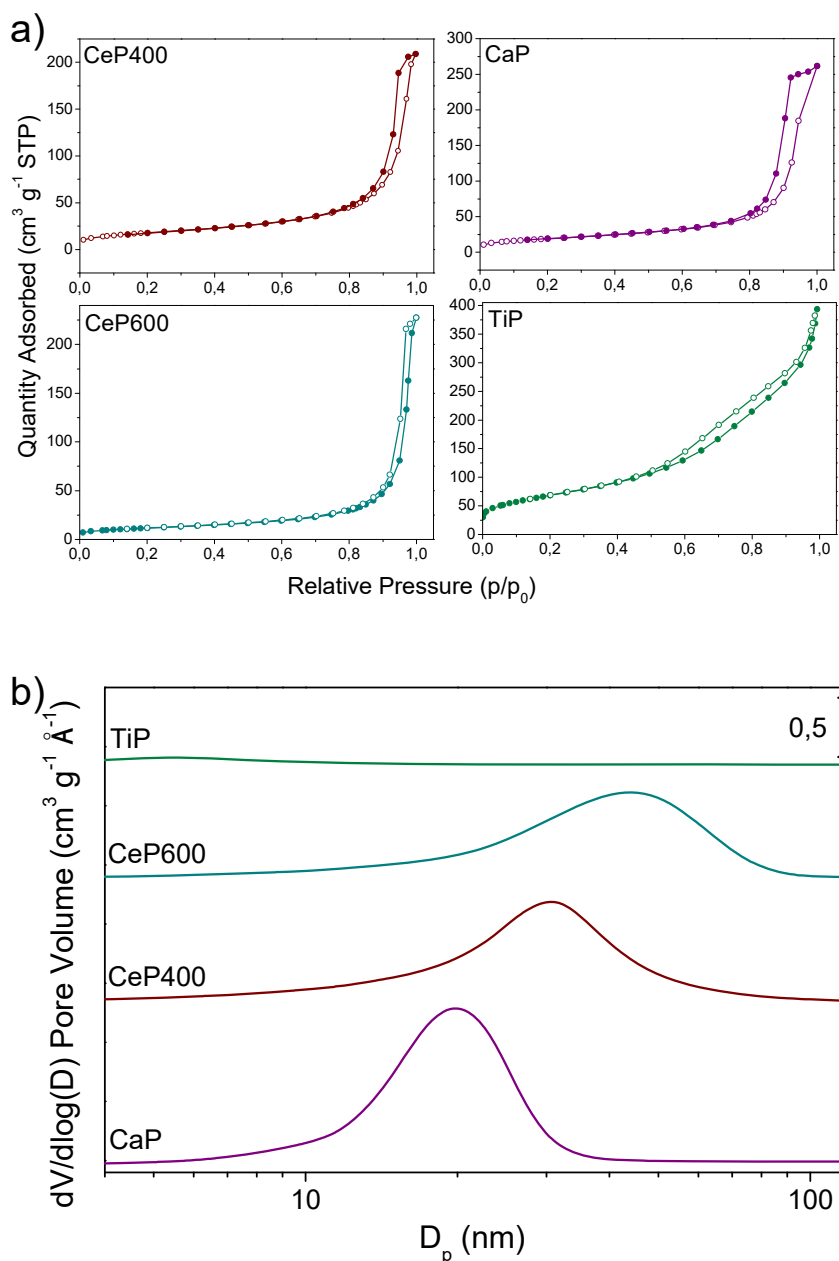
Figure 2. a) Nitrogen adsorption/desorption isotherms and b) BJH pore size distribution of the supports after calcination.

Figure 3 shows the TEM micrographs (Fig. 3a) and the Pt particle size distribution (Fig. 3b) of the prepared catalysts. In the rhabdophane-type phase of $CePO_4$, the particles are bar-shaped with a length of ca. 120 nm. The oxygen atoms of the structure are forming a series of parallel channels along the *c* axis, in which water molecules can be accommodated [21, 30-32]. The bar-like structure of the support is maintained after calcination at 600 °C, but a decrease of the bars length takes place, along with the

disappearance of the structural channels, due to the formation of the monazite-type phase of $CePO_4$ [21]. Calcium hydroxyapatite consists in bar-like particles of ca. 38 nm, with structural channels along the hexagonal axis, well known for their capacity of trapping molecules [41], whereas support TiP present an irregular shape and no cavities are observed in its structure. The Pt species are highly dispersed on these solids, in good agreement with the XRD results, with particle sizes between 0.7 and 2.6 nm. However, supports with structural channels CeP and CaP show narrower particle size distributions, as well as a preferential arrangement of the Pt particles in the direction of the structural channels. This could be attributed to the structural characteristics of the support. Well-ordered channel structures have demonstrated to favor good dispersion of the metal particles, as well as prevent them of sintering [42]. Figure 4 shows the mean Pt particle size in each catalyst as a function of the mean pore diameter of the corresponding support calculated by N_2 physisorption, pointing out the influence of the porosity in the metal particle size control. As the support mean pore diameter increases, a decrease of the mean Pt particle size occurs, probably due to the inclusion of the metal particles into the pores, presenting those supported on channel-containing supports the smallest size.
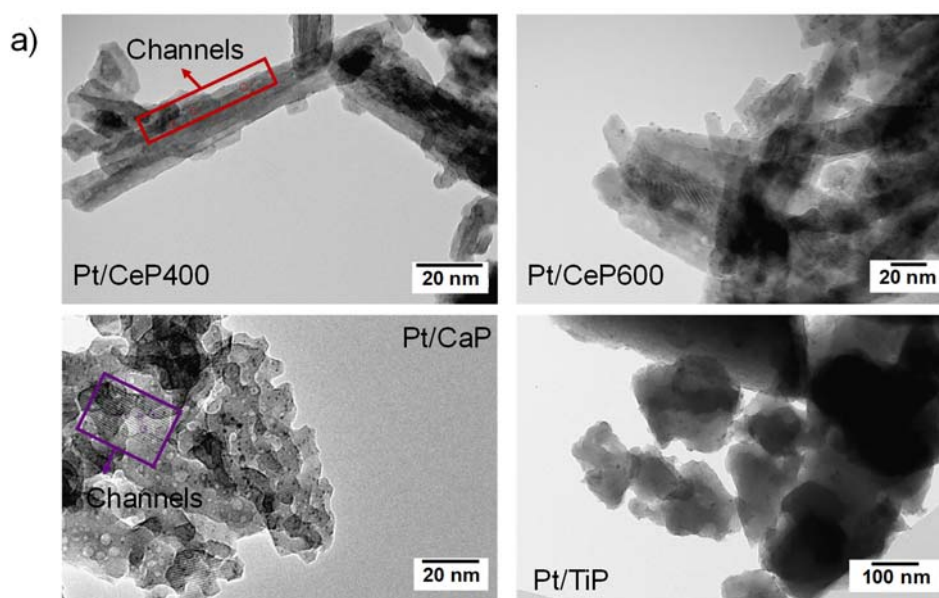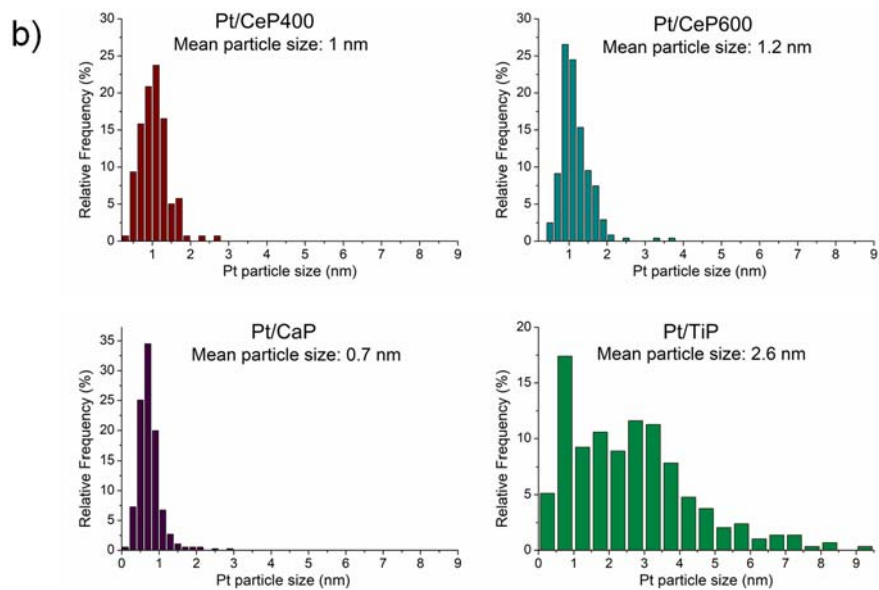
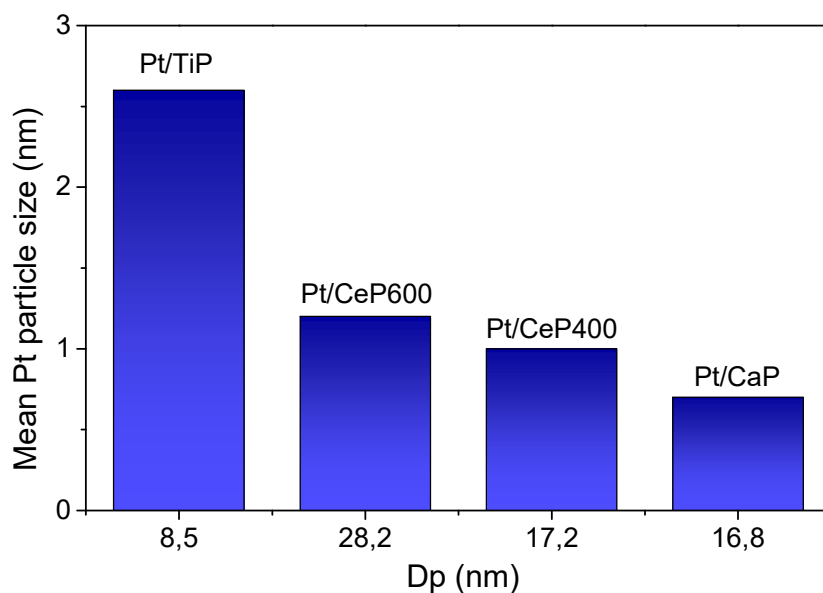**Figure 3.** a) TEM micrographs and b) particle size distribution of the prepared catalysts.

Figure 4. Mean Pt particle size of the catalysts as a function of the support pore diameter.

3.2. Catalytic test

Firstly, supports in the absence of metal phase present no activity towards the WGS reaction. Figure 5 shows the catalytic activity results of the Pt catalysts. The catalytic performance of the evaluated solids decreases in the order: Pt/CaP > Pt/CeP400 > Pt/CeP600 > Pt/TiP. Whereas the catalyst Pt/CaP reaches the equilibrium conversion at

310 °C, those supported on CeP achieve it at 350 °C, and the Pt/TiP catalyst present a limited catalytic activity, with a CO conversion value lower than 10% at 350 °C. This result could be attributed to the mean Pt particle size in every sample as well as to the interaction of the support with the water molecule during the reaction, directly related with the pore size and volume of each support as confirmed by the N_2 physisorption results. The trend followed by the Pt catalysts indicates that supports with structural channels, rather those supported on CaP or CeP, lead to an enhancement of the catalytic behavior. Considering that CO_2 and H_2 are potential reactants for the methanation reaction, it has been generally reported that their presence induces a negative effect on the WGS catalytic activity [43]. However, no methane was detected at the reactor outlet with the studied phosphate-supported catalysts. The catalytic activity of Cu-based LT (HiFuel W220) and MT (HiFuel W230) WGS commercial catalysts (Alfa Aesar™) is showed for comparison. The commercial catalysts exceed the activity of the Pt/TiP catalyst in all the temperature range evaluated, and those of the remaining solids in the temperature range between 150 and 290 °C. However, from 310 °C, the catalysts Pt/CaP and Pt/CeP400 exceed the CO conversion achieved by the commercial catalysts, whereas the system Pt/CeP600 becomes more active than the catalyst HiFuel W230 and equal to the catalyst HiFuel W220 from 330 °C. Furthermore, none of the commercial catalysts reach the equilibrium conversion in the evaluated conditions, in contrast to the CaP and CeP supported catalysts. These results point out the suitability of the studied phosphate-based systems for the WGS reaction, particularly those containing channels, that is CaP and CeP400.
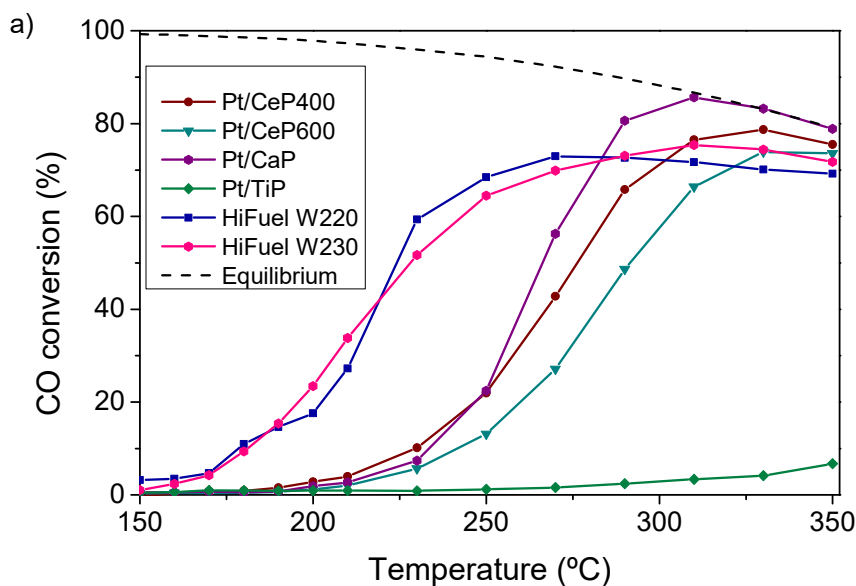
Figure 5. CO conversion of phosphate-supported Pt catalysts and commercial catalysts as a function of the reaction temperature under a feed-stream containing 7% CO, 9% CO_2, 30% H_2O, 50% H_2 and 4% N_2. WGS equilibrium curve is also presented.

A correlation between the catalysts pore volume and the temperature at which they reach a particular value of CO conversion value is shown in Figure 6. Given that the description of the porosity of Pt/TiP is not representative of the real characteristics of the material, which presents mainly micropores, this correlation is not presented for this catalyst. However, it exists a clear connection between the mesopore volume of the remaining catalysts and their catalytic activity, demonstrating that an increasing mesopores population in the solid gives place to a decrease of the temperature at which they reach a certain conversion value. Whereas the catalyst Pt/CeP600, with a lower pore volume, requires higher temperatures, the catalysts whose supports present structural channels, and hence a superior pore volume, lead to an improvement of the catalytic activity, which is consistent considering that the porosity of the support seems to influence the interaction of the catalyst with the water molecule and consequently the availability of water during the WGS reaction [21].
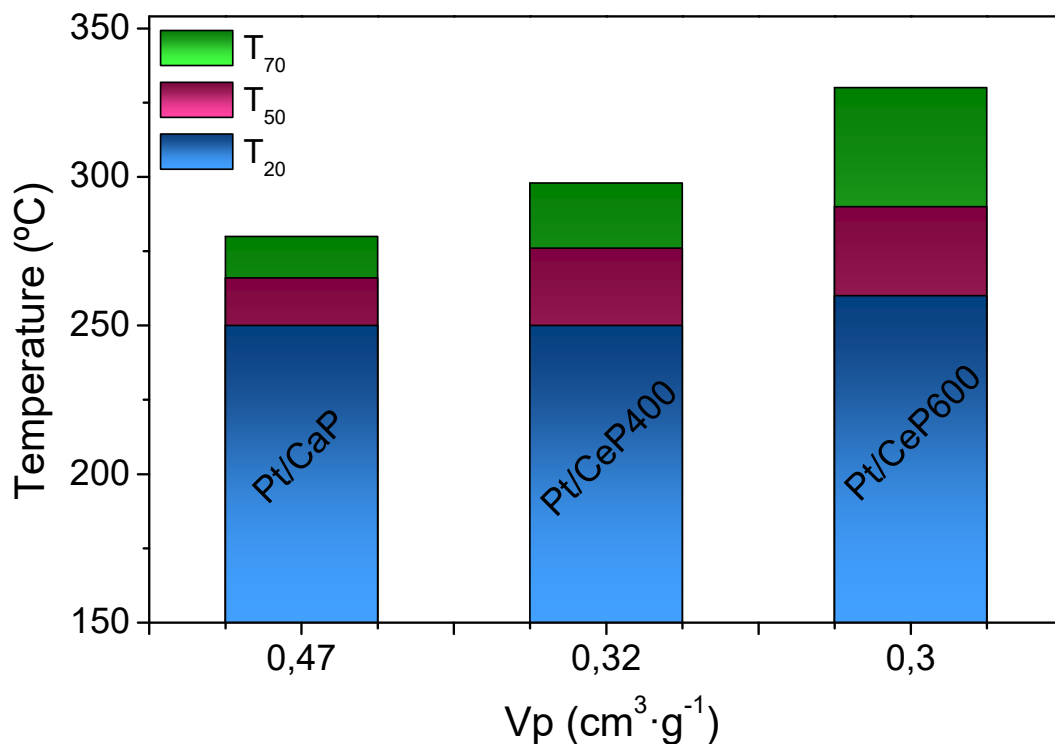
Figure 6. Temperature at which Pt catalysts reach a 20 (T_{20}), 50 (T_{50}) and 70% (T_{70}) of CO conversion as a function of the pore volume of the catalysts.

Water adsorption experiments (10% H_2O/Ar) followed by DRIFTS and mass spectrometry were carried out in order to understand the influence of the water-support interaction on the WGS catalytic performance. DRIFT spectra of the evaluated supports after the activation treatment are presented in Figure 6. The CeP and CaP spectra show a band at ca. 5300 cm^{-1}, which confirms the presence of water on these solids even after the activation treatment. Every support present bands in the OH stretching region, indicating the presence of structural surface OH groups. Whereas the solids CeP and TiP show only a band at 3670 cm^{-1}, the support CaP present several bands in this spectral region. While the band at 3568 cm^{-1} has been attributed to the stretching vibration of OH ions on lattice sites of the hydroxyapatite structure [34, 44, 45], a series of weak bands at higher wavenumbers are observed, which have been assigned previously to either surface $Ca(OH)_2$ or surface P-OH groups. Particularly the band at

3660 cm^{-1} could appear due to the presence of P-OH groups belonging to surface acidic phosphate ions HPO$_4^{2-}$, since a band at this frequency has been observed in phosphoric acid impregnated silica gels [44, 46]. According to the presence of phosphate groups in the studied supports, bands in the 900-1100 cm^{-1} region are expected. Thus, the band at 960 cm^{-1} in the spectra of CeP and CaP corresponds to the symmetric P-O stretching mode (v_1). Bands at 1028 and 1090 cm^{-1} are also observed for CeP400 and CeP600 respectively, assigned to the asymmetric P-O stretching modes (v_3). Nevertheless, the CaP spectrum presents several bands between 1016 and 1083 cm^{-1}. Both the differences on the vibration frequency values and the number of bands in this region indicate different degree of distortion of the PO$_4^{3-}$ tethraedra as a consequence of the phosphate group environment in every solid [21, 47]. Bands at 1185, 1173 and 1230 cm^{-1} appear for the systems CeP, CaP and TiP respectively, corresponding to the P=O stretching mode [48, 49]. The shift of this band in the solid TiP towards higher wavenumbers is related to the deformation of the P=O bonds by the Ti-O environment [37]. In the crystalline solids, that is CeP and CaP, a set of bands appears in the 2100-2400 cm^{-1} range, ascribed to overtone and combination bands of the phosphate vibrations [47], whereas the band at 2884 cm^{-1}, only present in CeP400, correspond to the P-OH stretching mode characteristic of acid ortophosphates (PO$_4^{3-}$ + H$_2$O) [21, 48]. Regarding the CaP system, it is known that hydroxyapatites are characterized by the substitution of OH$^-$ or PO$_4^{3-}$ groups by CO$_3^{2-}$ groups, giving rise to the so called type A and type B substitution respectively [50]. Therefore, vibrations corresponding to the CO$_3^{2-}$ group are present. A-type carbonate species in apatite structures are characterized by absorption bands at 1545 and 1450 cm^{-1}, corresponding to the asymmetric and symmetric stretching respectively, and a singlet at 880 cm^{-1}, whereas the B-type carbonate species are expected at 1455, 1410 and 875 cm^{-1}. In our sample, two intense bands at 1417 and 1448 cm^{-1}are observed, as well as a singlet at 872 cm^{-1}, which allows to conclude that a type B substitution has taken place in this solid [34]. The presence of carbonate groups could also explain the appearance of a shoulder at 3535

cm^{-1} in the OH stretching region, that has been previously attributed to surface OH groups locally perturbated by the presence of CO_3^{2-} groups [45].
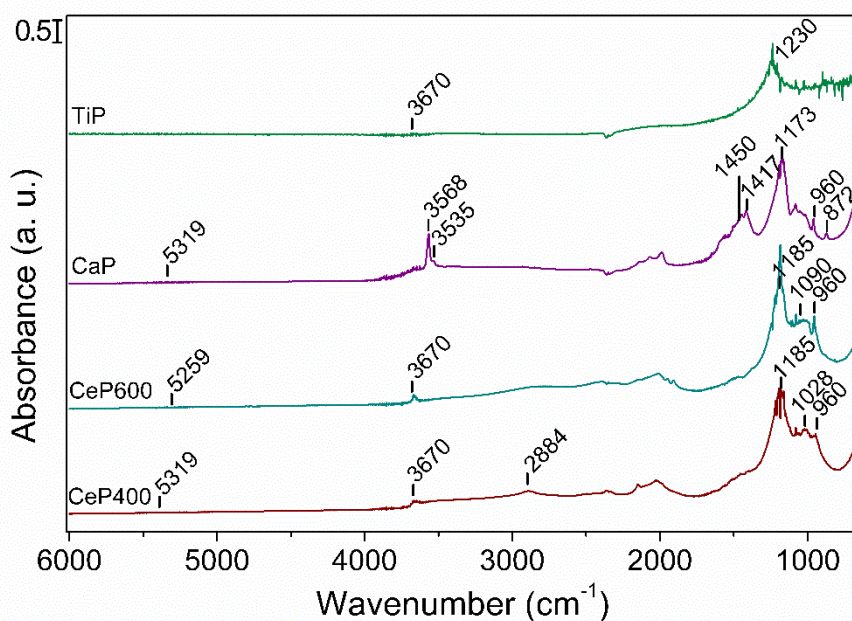

Figure 6. DRIFT spectra of the studied supports after the activation treatment under 10% H$_2$/Ar.

The behavior of the surface species in the presence of water was analyzed through the monitoring of the water adsorption experiments. Difference spectra of the supports are presented in figure 7. Every spectra except that of TiP show the growth of the bands at ca. 5300 cm^{-1} corresponding to water combination bands ($v + \delta$(H$_2$O)). Nevertheless, its intensity is greater for the CeP solids than for CaP in all the temperature range. The supports CeP and CaP present an additional band in this region at relatively low frequency ($\sim$ 5200 cm^{-1}), which indicates the presence of H-bonded H$_2$O species [51]. A weak and broad band about 4000 cm^{-1} is observed for CeP400 and CeP600, where combination modes of the -OH groups ($v + \delta$(OH)) appear. Regarding the -OH stretching region, the band at 3670 cm^{-1} in both the spectra of CeP400 and CeP600 is shifted to 3690 cm^{-1} in the presence of water, indicating that this -OH groups are participating in the hydrogen bonding. As the temperature increases, the availability of water in these solids decreases [21] and consequently the amount of hydrogen bonds, thus the -OH

band frequency is shifted progressively towards lower wavenumbers. A similar behavior is observed for CaP, being the band at 3568 cm^{-1} shifted towards higher wavenumbers in the presence of water. However, in this support a series of bands in the 3750-3600 cm^{-1} range appear when water is adsorbed, denoting the generation of new -OH groups and thus exposing the ability of the hydroxyapatite for dissociating the water molecule, in contrast to the behavior showed by the CeP supports, where water species remain as molecular water [21]. Since proton conductivity has demonstrated to play a fundamental role on the WGS catalytic performance [20], this result allows to conclude that a Grotthuss mechanism takes place in the support CaP, i. e., the water molecules show pronounced local dynamics but they stay at their sites, being the protons transferred within hydrogen bonds from one molecule to another. Additionally, a reorganization of the proton environment occurs forming a trajectory for proton migration. In the case of the supports CeP, a diffusion mechanism occurs, meaning that the proton transport is assisted by the translational dynamics of the water molecule [23, 52]. Liu et al. [53] have demonstrated that proton conduction properties can be tuned by controlling the crystal structure, porous network and chemical functionality of the conductor solids, thus, the differences observed in the studied phosphate-type supports can be ascribed to the differences in their crystallographic structure and porosity. All the evaluated supports present also bands between 3500 and 2500 cm^{-1} characteristic of adsorbed molecular water. This band is particularly weak in the support TiP, which shows the low affinity of water by this support and explains the low activity of the Pt/TiP catalyst on the WGS reaction. Although this support presents the greatest specific surface area value, the loss of phosphorous and the absence of mesopores in its structure suppose a poor interaction with the water molecule. The observation of the H-O-H bending mode (δ_{H-O-H}) region allows to determine also the type of interaction between the water molecule and the surface. Since the water molecule is amphoteric, it is able to interact with both acidic surface sites (through the lone pair electrons of the oxygen atom) and with basic sites (through the formation of hydrogen bonding). When the interaction occurs via hydrogen

bonding, the δ_{H-O-H} mode shifts to higher wavenumbers while the interaction via the oxygen atom produces a shift of the δ_{H-O-H} mode towards lower wavenumbers [51, 54, 55]. According to that, the water in the solids CeP400 and CeP600 are interacting through hydrogen bonding, due to the high H-O-H bending mode frequencies at 1625 and 1630 cm^{-1} respectively. CeP400 spectrum shows also a band at 1586 cm^{-1} as the temperature increases. Falk et al. [55] found a relationship between the δ_{H-O-H} frequency shift and the formal charge of the cation with which the water molecules were interacting. For the cation Ce^{3+} this value would be found at ca. 1532 cm^{-1}, a value much lower than that found in our sample, thus this vibration mode has been assigned to the structural water present in the structural channels of the rhabdophane-type phase of CePO$_4$ [21]. The spectrum of CaP shows two different contributions, one at 1642 cm^{-1}, corresponding to the bending mode of hydrogen-bonded species and another one at 1568 cm^{-1}. The average value of the δ_{H-O-H} mode interacting with a cation with charge 2+ should appear at 1560 cm^{-1}, close to the value found for this mode in the CaP spectrum. Consequently, this vibration could be assigned to that of the water molecules interacting via the lone electron pair of oxygen with the Ca^{2+} ions of the hydroxyapatite structure. This band remains even at 350 °C, exposing that this interaction is stronger than that via hydrogen bonding.
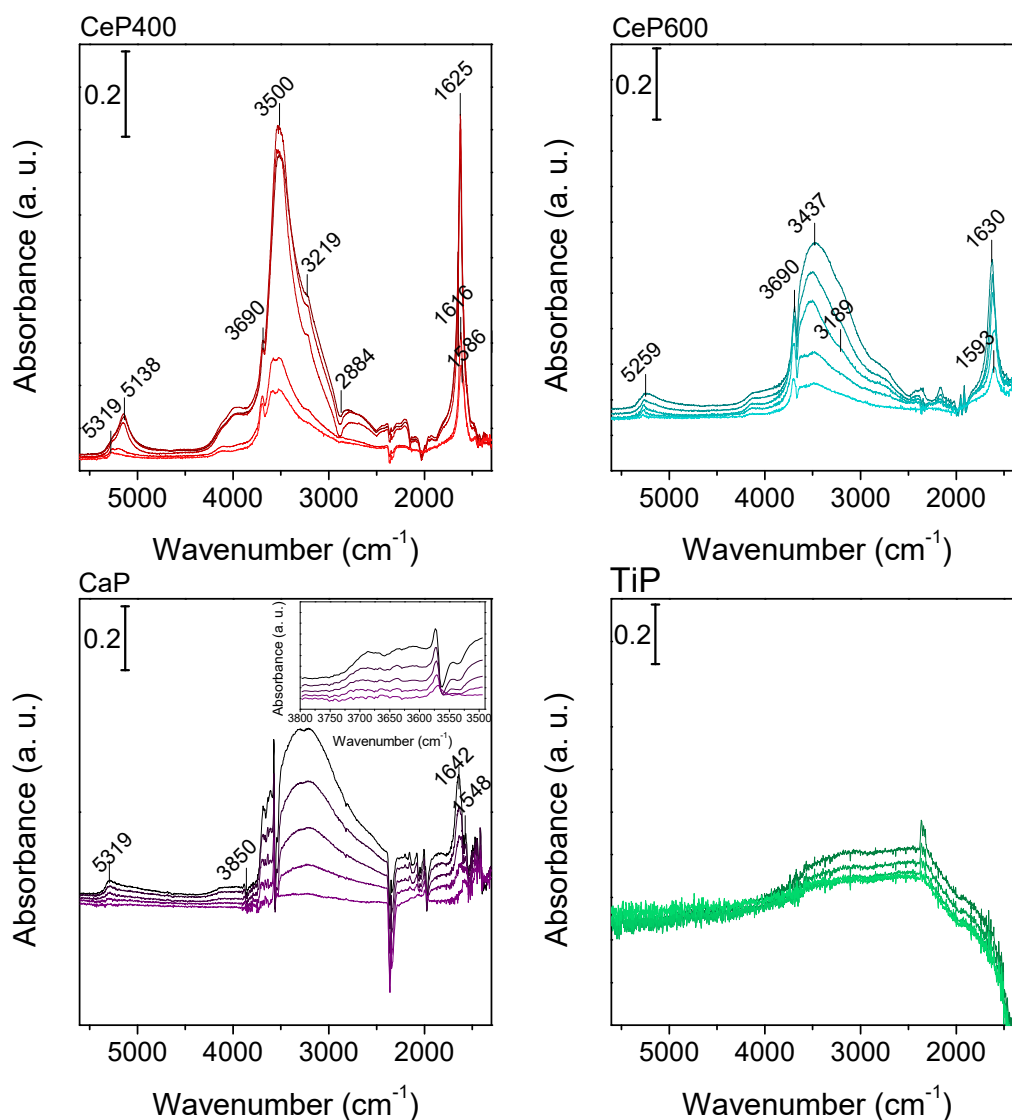
Figure 7. Evolution of the DRIFT spectra of the supports during the adsorption of 10% H_2O/Ar, from 150°C (top) to 350°C (bottom).

The evolution of the relative intensity of the mass-on-charge (m/z) 18 during the water adsorption experiments were followed by mass spectrometry. The results are showed in Figure 8. Water retention capacity of the evaluated supports decreases in the order: CaP > CeP400 > CeP600 > TiP, which coincides with the trend followed by the corresponding catalysts on the WGS reaction. The support CaP shows an excellent water adsorption capacity, being able to greatly retain the water in the whole temperature range evaluated. This fact can be attributed to the interaction of the water molecule not only with the

phosphate and -OH groups but also with the Ca^{2+} ion, as proved by DRIFTS. This result is in agreement with previous studies, which have demonstrated that calcium hydroxyapatite interacts strongly with the water molecule through electrostatic/hydrogen bonding with the Ca^{2+} and phosphate ions of the apatite surface. Furthermore, the charge density on the Ca^{2+} ions are more localized than on the phosphate groups in the presence of water, provoking a dramatical decrease on the water molecule mobility in the proximity of the apatite surface and thus favoring the retention of water on the structure even at high temperatures [56-58]. However, the support CeP400 reaches a maximum adsorption capacity at 250 °C, which decreases when this temperature is exceeded. As previously reported [21], the hexagonal structure of $CePO_4$ has demonstrated a great interaction ability with the water molecule that has been attributed to the interaction of the latter with the phosphate groups of the support and the influence of their structural -OH groups. Therefore, the greater interaction of the water molecule with the solid CaP with respect to CeP400 is explained by the interaction of H_2O with the Ca^{2+} ions, much stronger than the interaction with the surface phosphate or -OH groups. In addition, considering that the support CaP contains a greater pore volume than CeP400, the interaction of water with the channels of this solid is favored. The support CeP600 shows a great affinity for water, although its adsorption capacity starts to decrease at 200 °C and is lower than that of CeP400 in all the temperature range. In spite of the interaction of the surface phosphate groups of the monoclinic phase of $CePO_4$ with the water molecule, the absence of the structural channels present in the hexagonal phase gives rise to a diminishing of the strength of this interaction. Finally, the support TiP presents a strong adsorption of water at 150 °C, which decreases drastically while the temperature increases. This fact could be attributed to the loss of phosphorous in this support during the calcination procedure and the consequent impossibility of the water molecule to interact with the phosphate groups. Thus, the water retention capacity of the supports is directly related with the catalytic trend observed for

the Pt catalysts in the WGS reaction and also with the selectivity of the reaction. These results evidence the fundamental role of the water availability for an enhanced WGS catalytic performance, demonstrating that the WGS reaction could be improved through the modulation of the structural characteristics of the employed phosphate-type supports.
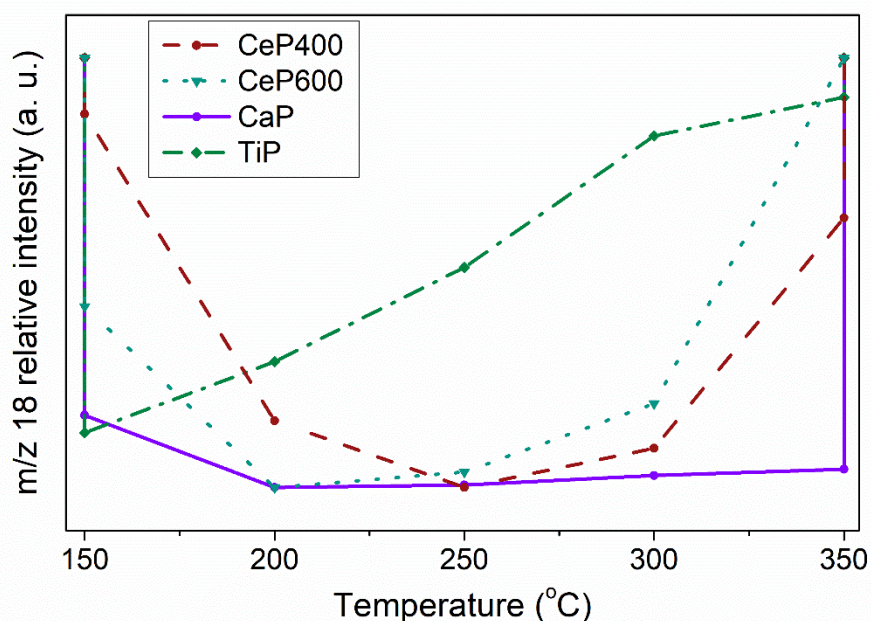

Figure 9. Evolution of the mass-on-charge (m/z) 18 as a function of the temperature during the adsorption of 10% H_2O/Ar.

4. Conclusions

A series of phosphate-based compounds containing Ca, Ce and Ti have been used as supports for Pt catalysts and evaluated on the WGS reaction. Considering that the availability of water plays a fundamental role in the WGS reaction mechanism, the structure and water adsorption capacity of these supports have been related to the WGS catalytic performance. Results show that catalytic activity decreases in the order: Pt/CaP > Pt/CeP400 > Pt/CeP600 > Pt/TiP. Supports containing structural channels, that is CaP and CeP400, favor the adsorption of water through the interaction with the phosphate groups contained on them. Nevertheless, the strong interaction of the water molecule

with the Ca^{2+} ion in CaP explains the superior catalytic activity of this system. When channels are not present in the phosphate structure, as ocurring in the support CeP600, the interaction of water with the phosphate groups is weakened and thus the catalytic activity decreases. Finally, the support TiP experienced a loss of phosphorous during the calcination procedure, decreasing the surface phosphate population and consequently, the interaction with the water molecule and the WGS catalytic activity. These results expose that phosphate-type compounds constitute appropriate supports for WGS catalysts, allowing to enhance their interaction with the water molecule during the reaction through the tuning of their surface and structural properties.

5. References

1. Liang, S. and G. Veser, *Nanocatalysts for the water gas shift reaction.* Nanomaterials and Energy, 2011. **1**: p. 117-133.
2. González-Castaño, M., et al., *Structuring Pt/CeO2/Al2O3 WGS catalyst: Introduction of buffer layer.* Applied Catalysis B: Environmental, 2017. **200**: p. 420-427.
3. Reina, T.R., et al., *Boosting the activity of a Au/CeO 2 /Al 2 O 3 catalyst for the WGS reaction.* Catalysis Today, 2015. **253**: p. 149-154.
4. Gonzalez Castaño, M., et al., *Pt vs. Au in water–gas shift reaction.* Journal of Catalysis, 2014. **314**: p. 1-9.
5. Price, C., et al., *Highly active Cu-ZnO catalysts for the WGS reaction at medium–high space velocities: Effect of the support composition.* International Journal of Hydrogen Energy, 2017. **42**(16): p. 10747-10751.
6. Vignatti, C., et al., *Catalytic and DRIFTS study of the WGS reaction on Pt-based catalysts.* International Journal of Hydrogen Energy, 2010. **35**(14): p. 7302-7312.
7. Panagiotopoulou, P. and D.I. Kondarides, *Effect of the nature of the support on the catalytic performance of noble metal catalysts for the water–gas shift reaction.* Catalysis Today, 2006. **112**(1-4): p. 49-52.
8. Olympiou, G.C., et al., *Mechanistic aspects of the water-gas shift reaction on alumina-supported noble metal catalysts: in situ DRIFTS and SSITKA-mass spectrometry studies.* Catalysis Today, 2007. **127**: p. 304-318.
9. Kalamaras, C.M., et al., *Effects of Reaction Temperature and Support Composition on the Mechanism of Water–Gas Shift Reaction over Supported-Pt Catalysts.* The Journal of Physical Chemistry C, 2011. **115**(23): p. 11595-11610.
10. González-Castaño, M., et al., *Deep insight into Zr/Fe combination for successful Pt/CeO2/Al2O3WGS catalyst doping.* Catal. Sci. Technol., 2017. **7**(7): p. 1556-1564.
11. Trovarelli, A., *Catalytic Properties of Ceria and CeO$_2$-Containing Materials.* Catalysis Reviews, 2006. **38**(4): p. 439-520.
12. Cargnello, M., et al., *Control of Metal Nanocrystal Size Reveals Metal-Support Interface Role for Ceria Catalysts.* Science, 2013. **341**: p. 771-773.
13. García-Moncada, N., et al., *New concept for old reaction: Novel WGS catalyst design.* Applied Catalysis B: Environmental, 2018. **238**: p. 1-5.
14. González-Castaño, M., et al., *Tailoring structured WGS catalysts: Impact of multilayered concept on the water surface interactions.* Applied Catalysis B: Environmental, 2018. **222**: p. 124-132.
15. Liu, P. and J.A. Rodriguez, *Water-gas-shift reaction on metal nanoparticles and surfaces.* J Chem Phys, 2007. **126**(16): p. 164705.
16. Phatak, A.A., et al., *Kinetics of the water–gas shift reaction on Pt catalysts supported on alumina and ceria.* Catalysis Today, 2007. **123**(1-4): p. 224-234.
17. González-Castaño, M., et al., *O 2 -assisted Water Gas Shift reaction over structured Au and Pt catalysts.* Applied Catalysis B: Environmental, 2016. **185**: p. 337-343.
18. Jain, R., et al., *Comparative study for low temperature water-gas shift reaction on Pt/ceria catalysts: Role of different ceria supports.* Applied Catalysis A: General, 2015. **507**: p. 1-13.
19. Pazmiño, J.H., et al., *Metallic Pt as active sites for the water–gas shift reaction on alkali-promoted supported catalysts.* Journal of Catalysis, 2012. **286**: p. 279-286.
20. García-Moncada, N., et al., *A direct in situ observation of water-enhanced proton conductivity of Eu-doped ZrO 2 : Effect on WGS reaction.* Applied Catalysis B: Environmental, 2018. **231**: p. 343-356.

21. Navarro-Jaén, S., et al., *Pt/CePO4 catalysts for the WGS reaction: influence of the water-supplier role of the support on the catalytic performance.* Journal of Materials Chemistry A, 2018.

22. Peighambardoust, S.J., S. Rowshanzamir, and M. Amjadi, *Review of the proton exchange membranes for fuel cell applications.* International Journal of Hydrogen Energy, 2010. **35**(17): p. 9349-9384.

23. Kreuer, K.-D., et al., *Transport in Proton Conductors for Fuel-Cell Applications: Simulations, Elementary Reactions, and Phenomenology.* Chemical Reviews, 2004. **104**: p. 4637-4678.

24. Iriarte-Velasco, U., et al., *Transition metals supported on bone-derived hydroxyapatite as potential catalysts for the Water-Gas Shift reaction.* Renewable Energy, 2017.

25. Ghahfarrokhi, A.M., P. Moshiri, and M. Ghiaci, *Studies on calcined cow bone and pyrolyzed wood, suitable supports for inmobilizing hybrid nanoparticles of Co-Mn as new catalysts for oxidation of 2,6-diisopropyl naphtalene.* Applied Catalysis A: General, 2013. **456**: p. 51-58.

26. Wijzen, F., et al., *Texture and Structure of Amorphous Co-Precipitated Silica-Aluminium Phosphate Catalyst Supports.* Journal of Catalysis, 1998. **177**: p. 96-104.

27. Kanai, S., et al., *A bifunctional cerium phosphate catalyst for chemoselective acetalization.* Chemical Science, 2017. **8**(4): p. 3146-3153.

28. Romero-Sarria, F., et al., *CO oxidation at low temperature on Au/CePO4: Mechanistic aspects.* Applied Catalysis B: Environmental, 2011. **107**(3-4): p. 268-273.

29. Ren, T.-Z., et al., *Tailoring the Porous Hierarchy of Titanium Phosphates.* Langmuir, 2006. **22**.

30. Horváth, I., A. Bondar, and L.P. Mezentseva, *Termochemistry of Hydrated Rare Earth Ortophosphates.* Journal of Thermal Analysis, 1988. **33**: p. 755-760.

31. Mooney, R.C.L., *X-ray Diffraction Study of Cerous Phosphate and Related Crystals. I. Hexagonal modification.* Acta Crystallographica, 1950. **3**: p. 337-340.

32. Mooney, R.C.L., *Crystal Structures of a Series of Rare Earth Phosphates.* The Journal of Chemical Physics, 1948. **16**(10): p. 1003-1003.

33. Boukha, Z., et al., *Methane dry reforming on Ni loaded hydroxyapatite and fluoroapatite.* Applied Catalysis A: General, 2007. **317**(2): p. 299-309.

34. Domínguez, M.I., et al., *Gold/hydroxyapatite catalysts: Synthesis, characterization and catalytic activity to CO oxidation.* Applied Catalysis B: Environmental, 2009. **87**(3-4): p. 245-251.

35. Wang, L., et al., *Structural and morphological transformations of mesostructured titanium phosphate through hydrothermal treatment.* J Colloid Interface Sci, 2007. **316**(2): p. 954-61.

36. Takahashi, H., T. Oi, and M. Hosoe, *Characterization of semicrystalline titanium(iv) phosphates and their selectivity of cations and lithium isotopes.* Journal of Materials Chemistry, 2002. **12**(8): p. 2513-2518.

37. Kőrösi, L. and I. Dékány, *Preparation and investigation of structural and photocatalytic properties of phosphate modified titanium dioxide.* Colloids and Surfaces A: Physicochemical and Engineering Aspects, 2006. **280**(1-3): p. 146-154.

38. Elliot, J.C., *Structure and Chemistry of the Apatites and other Calcium Ortophosphates*. 1994: Elsevier Science.

39. *Handbook of Heterogeneous Catalysis*. 2nd edition ed, ed. G. Ertl, et al. Vol. 1. 2008: Wiley-VCH.

40. Leofanti, G., et al., *Surface area and pore texture of catalysts.* Catalysis Today, 1998. **41**: p. 207-219.

41. *Hydroxyapatite and related materials*, ed. P.W. Brown and B. Constantz. 1994: CRC Press.

42. Parapat, R.Y., et al., *Support effect in the preparation of supported metal catalysts via microemulsion.* RSC Adv., 2014. **4**(92): p. 50955-50963.

43. Ratnasamy, C. and J.P. Wagner, *Water Gas Shift Catalysis.* Catalysis Reviews, 2009. **51**(3): p. 325-440.

44. Ishikawa, T., M. Wakamura, and S. Kondo, *Surface characterization of calcium hydroxylapatite by Fourier transform infrared spectroscopy.* Langmuir, 1989. **5**(1): p. 140-144.

45. Bertinetti, L., et al., *Surface Structure, Hydration, and Cationic Sites of Nanohydroxyapatite: UHR-TEM, IR, and Microgravimetric Studies.* Journal of Physical Chemistry C, 2007. **111**: p. 4027-4035.

46. Low, M.J.D. and P. Ramamurthy, *Infrared study of the surface properties of phosphoric acid impregnated silica.* Journal of Physical Chemistry, 1968. **72**: p. 3161-3167.

47. Baddiel, C.B. and E.E. Berry, *Spectra structure correlations in hydroxy and fluorapatite.* Spectrochimica Acta, 1966. **22**: p. 1407-1416.

48. Dayanand, C., et al., *Structural investigations of phosphate glasses: a detailed infrared study of the x(PbO)-(1-x)P2O5 vitreous system.* Journal of Materials Science, 1996. **31**: p. 1945-67.

49. Nazaraly, M., et al., *Synthesis and characterization of CeIV(PO4)(HPO4)0.5(H2O)0.5.* Journal of Physics and Chemistry of Solids, 2006. **67**(5-6): p. 1075-1078.

50. Berzina-Cimdina, L. and N. Borodajenko, *Infrared Spectroscopy- Materials Science, Engineering and Technology*, ed. T.M. Theophanides. 2012: InTech.

51. Vimont, A., et al., *Investigation on Acid Sites in a Zeotypic Giant Pores Chromium(III) Carboxylate.* Journal of the American Chemical Society, 2006. **128**: p. 3218-3227.

52. Kreuer, K.-D., *Proton Conductivity: Materials and Applications.* Chemistry of Materials, 1996. **8**: p. 610-641.

53. Liu, M., et al., *Three-dimensional protonic conductivity in porous organic cage solids.* Nat Commun, 2016. **7**: p. 12750.

54. Burneau, A., *Near infrared spectroscopic study of the structures of water in proton acceptor solvents.* Journal of Molecular Liquids, 1990. **46**: p. 99-127.

55. Falk, M., *The frequency of the H-O-H bending fundamental in solids and liquids.* Spectrochimica Acta, 1984. **40A**: p. 43-48.

56. Zahn, D. and O. Hochrein, *Computational study of interfaces between hydroxyapatite and water.* Physical Chemistry Chemical Physics, 2003. **5**(18): p. 4004.

57. Zhao, W., et al., *Surface energetics of the hydroxyapatite nanocrystal-water interface: a molecular dynamics study.* Langmuir, 2014. **30**(44): p. 13283-92.

58. Bolis, V., et al., *Coordination chemistry of Ca sites at the surface of nanosized hydroxyapatite: interaction with H(2)O and CO.* Philos Trans A Math Phys Eng Sci, 2012. **370**(1963): p. 1313-36.